Permeance Distribution Function: A Powerful Tool to Analyze Electromagnetic Forces Induced by PWM Current Harmonics in Multiphase Surface Permanent-Magnet Motors

Yajun Lv, Siwei Cheng, *Member, IEEE*, Zhongkun Ji, Dong Wang, *Member, IEEE*, and Junquan Chen, *Member, IEEE*

***Abstract*—This article introduces a new method to analyze electromagnetic forces induced by pulsewidth modulation current harmonics in inverter-fed surface permanent-magnet motors. The concept of the permeance distribution function (PDF) is first introduced with its properties and relation to machine inductances fully explained. Utilizing the concept of PDFs, two methods are proposed to calculate the flux distribution on stator boundaries by armature currents and rotor permanent magnets, respectively. By superposing the stator flux distributions from both sources, the final stator electromagnetic force distribution is obtained. The method is validated by finite-element analysis, demonstrating good accuracy and very fast computation time.**

***Index Terms*—Current harmonics, electromagnetic force, finite-element analysis (FEA), noise and vibration harshness, permanent-magnet synchronous machine (PMSM), permeance distribution function, pulsewidth modulation (PWM), radial magnetic force (RMF), relative permeance, surface permanent-magnet motor (SPM), vibration and acoustic noise.**

I. Introduction

PERMANENT-MAGNET synchronous machines (PMSMs) have been extensively used nowadays in energy industries, transportations, advanced manufacturing, and defense industries. Compared with conventional three-phase PMSMs, multiphase PMSMs have a more sinusoidal magneto motive force (MMF) and, thus, generally exhibit less torque ripple and a cleaner spectrum of radial magnetic forces (RMFs) [1], [2]. Such advantages have made them the preferred choice for many vibration–critical applications, such as vessel propulsions, high-precision servos, and electric vehicle drives [3], [4].

Manuscript received July 31, 2019; revised October 26, 2019; accepted December 4, 2019. Date of publication December 16, 2019; date of current version March 13, 2020. This work was supported in part by the National Science Foundations of China under Grants 51977215, 51825703, and 51690181. Recommended for publication by Associate Editor K. Akatsu. *(Corresponding author: Siwei Cheng.)*

The authors are with the National Key Laboratory of Science and Technology on Vessel Integrated Power System, Naval University of Engineering, Wuhan 430033, China (e-mail: yajunlv@163.com; siwei_cheng@sina.com; zhongkunji@163.com; wangdongl@vip.sina.com; 303972127@qq.com).

Color versions of one or more of the figures in this article are available online at http://ieeexplore.ieee.org.

Digital Object Identifier 10.1109/TPEL.2019.2960568

Although multiphase PMSMs can be designed with very low torque ripples and thus have good low-frequency vibration performance, their high-frequency vibration performance is limited by output current harmonics of the connected pulsewidth modulation (PWM) inverters [5]–[7]. In hybrid/electric vehicles, for example, the whining sound emitted by inverter-fed motors has been a difficult noise and vibration harshness problem [8].

To study high-frequency motor vibrations and acoustic noises, the first crucial step is to accurately calculate machine internal electromagnetic (EM) forces induced by the PWM current harmonics. Traditionally, it is believed that the RMF is mainly responsible for PWM-induced high-frequency vibrations of PMSMs [6], [9]–[11]. The RMF is normally calculated from the machine airgap flux distribution, which can be efficiently calculated by analytical methods, such as the MMF-based method, the complex relative airgap permeance method, or the subdomain method [12]–[14], if the magnetic saturation of the machine is ignored. Once the airgap flux distribution is obtained, the RMF can be determined by extracting the radial component of the Maxwell stress tensor along the airgap circle.

However, it should be pointed out that the RMF along the airgap circle is only a crude approximation of the overall force exerted on the stator bore [15]–[17]. It does not represent the realistic EM force distribution exerted on all the actual components of the stator. For many applications where only EM forces of low-spatial orders are concerned, such as those produced by permanent magnets (PMs) or by fundamental armature currents, the RMF calculated from the airgap flux is often adequate when used to predict the vibration of the PMSM either qualitatively or semiquantitatively [15], [18].

However, for applications where EM forces of high-spatial orders are concerned, such as those caused by high-frequency PWM current harmonics, the RMF calculated from the airgap flux is no longer effective in predicting the vibration of the PMSM.

To illustrate this point, Fig. 1 shows the instantaneous flux distribution of a six-phase concentrated-winding surface permanent-magnet motor (SPM) excited only by *the fundamental component of armature currents*. The instantaneous slot

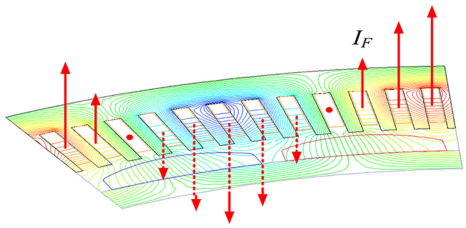

Fig. 1. Flux lines of a six-phase SPM under fundamental current excitations given by FEA.

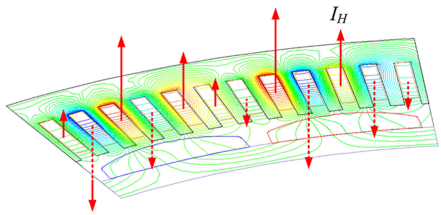

Fig. 2. Flux lines of a six-phase SPM excited by a single PWM current harmonic at the frequency of $(2f_s - f_e)$.

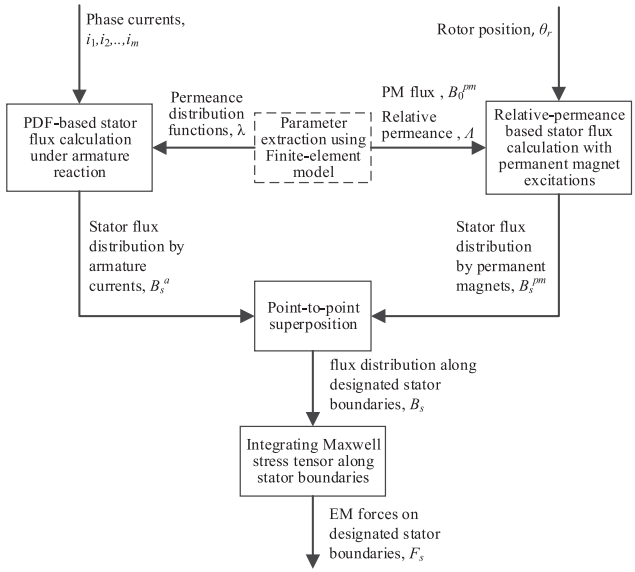

Fig. 3. Overall architecture of the PDF-based stator force calculation method.

currents, represented by red arrows in the figure, follow a sinusoidal spatial distribution.

As can be seen from the plot, the spatial order of the flux distribution is the same as the number of poles. Among all fluxes produced by armature currents, a good portion is the main flux that passes through the airgap. Therefore, although it is not exactly accurate to use the airgap RMF to characterize the force seen by the stator, the error is generally acceptable for the purpose of assessing motor vibrations.

On the contrary, Fig. 2 shows the instantaneous flux distribution of the same SPM excited by *a single PWM current harmonic* with PWM carriers shifted by 105° between two sets of three-phase windings. For this particular current harmonic, the instantaneous slot currents are distributed much more irregularly. Currents of adjacent slots often have opposite directions. Consequently, the resulting flux distribution is vastly different from that produced by the fundamental current. The spatial order of the flux distribution is now almost as high as the number of slots. The main flux that passes the airgap only makes up a tiny portion among all fluxes produced by armature currents, whereas the majorities are the slot leakage flux and the tooth-top leakage flux.

Apparently, the airgap RMF is no longer suitable to characterize the stator force caused by PWM current harmonics. Instead, the realistic stator force distribution can only be obtained by solving the actual EM forces on stator teeth boundaries and on stator coils.

To achieve this goal without resorting to brutal-force finite-element analysis (FEA), this article introduces a new motor parameter, the permeance distribution function (PDF). *The PDF is a distributed parameter that describes the flux distribution pattern on designated boundaries of the motor under the excitation of one phase current*. The parameter can be extracted by FEA for just once and then be used recursively to synthesize the time-varying flux distribution induced by all phase currents on all physical boundaries of stator teeth or inside stator slots. Therefore, not only it can one quantify the radial and lateral EM forces seen by the stator teeth caused by leakage fluxes, but it can also be able to calculate EM forces on the stator coils, which enables more precise analysis of PWM-harmonic-induced motor vibrations in the future.

This article is organized as follows. Section II formulates the problem and outlines the overall solution process. Section III introduces the concept of the PDF and discusses its properties and relation to machine inductances. Section IV explains how to use PDFs to calculate the stator flux distribution by armature currents. Section V explains how to calculate the stator flux distribution by PMs. Section VI combines the stator flux distributions from both sources and calculates the stator EM force distribution. Section VII concludes this article and outlines the future work.

II. Problem Formulation

Given a specific design of an SPM, this article aims to develop an efficient method to calculate EM forces seen by the stator teeth and the stator coils with known phase current waveforms and rotor position. The phase currents can be obtained beforehand from analytical analysis, dynamic-model simulations, or experimental measurements.

The method does not restrict harmonic contents of the phase currents nor does it require the phase currents to be completely balanced. However, since the proposed method is based on superposition principle, it does require that the magnetic saturation of the studied motor is within moderate levels so that the magnetic circuit is approximately linear. One must note that this assumption is no stronger than any other analytical method for solving magnetic fields inside electric machines.

The overall architecture of the proposed method is shown in Fig. 3. The finite-element model of the SPM is evaluated to extract the PDFs along designated stator boundaries, the PM

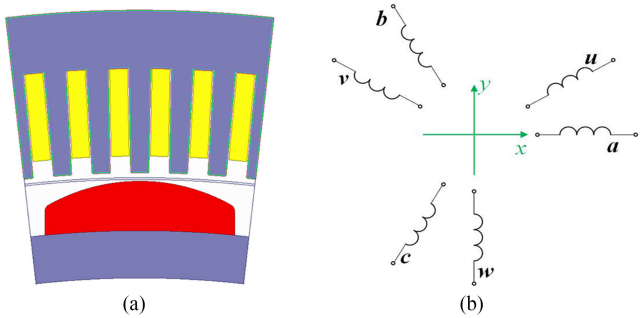

Fig. 4. Example six-phase concentrated-winding SPM. (a) Cross section. (b) Winding diagram.

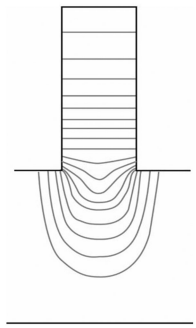

Fig. 5. Typical phase-current-induced flux distribution near the slot opening of a motor with a large airgap.

TABLE I
MAIN DESIGN PARAMETERS OF THE EXAMPLE MOTOR

Parameters	Symbols	Value	Unit
Number of phases	m	6	
Number of pole pairs,	P	14	
Number of slots per pole per phase	q	1	
Coil pitch	y	6	
Motor axial length	l	1430	mm
Stator inner diameter	D_s	1112	mm
Tooth width	b_t	18.79	mm
Slot width	b_s	22.8	mm
Slot depth	h_s	112	mm
Coil height	h_1	94.5	mm
Number of parallel branches	a	4	
Number of conductors per slot	N_s	16	
Rated current	I_{rms}	1343.5	A
Rated current angle relative to d-axis	γ	110	deg
Rated frequency	f_e	46.67	Hz
Sampling frequency	f_s	1000	Hz

flux distribution along the slotless stator bore, and the relative permeance due to the slotting effect.

Then, an analytical model based on PDFs is established to calculate the flux distribution along stator boundaries from armature currents. Furthermore, another analytical model based on the relative permeance along the stator bore is formed to calculate the stator flux distributions from PM excitations.

Results from both models are then superposed in a point-to-point fashion to obtain the combined stator flux distributions. Finally, by integrating the Maxwell stress tensor along designated stator boundaries, radial and lateral EM forces on stator teeth, as well as EM forces on stator coils, can be obtained.

To illustrate the proposed method, a six-phase concentrated-winding SPM with rectangular slots is taken as an example, as shown in Fig. 4. Parameters of the studied motor are shown in Table I.

To avoid unnecessary complications to the analysis, the following assumptions are made regarding the example motor.

1) Turn-to-turn insulations in the slot are neglected, i.e., all conductors in each slot are treated as a single large homogeneous conductor.
2) The skin effect and proximity effect on stator turns are neglected, i.e., the slot current is evenly distributed in the conductor.
3) Subtle geometric features of stator teeth, such as the wedge holder near the slot opening, are neglected. Hence, stator teeth have perfectly straight edges.
4) The two edges of a stator tooth are assumed to be approximately parallel when calculating the lateral force on the stator tooth.

III. PERMEANCE DISTRIBUTION FUNCTION

A. Definition

Inductances are important lumped parameters of electric machines, from which the main flux and the leakage flux can be calculated. However, knowing the magnetic flux and its composition is not enough to calculate the stator EM forces.

Fig. 5 shows the typical phase-current-induced flux distributions near the slot opening of a motor with relative large airgap. As can be seen from the plot, all flux lines can be classified as the leakage flux. However, some of the flux lines exit from the tooth top and thus results in a radial pulling force on top of the stator tooth. Other flux lines exit from tooth edges and are more concentrated near the slot opening. This part of the leakage flux results in a lateral pulling force distributed on the edge of the stator tooth.

Clearly, inductances as lumped machine parameters simply lack the information to describe the spatial distribution of stator forces. To overcome this limitation, some parameters with inherent information on flux distribution pattern on stator boundaries have to be introduced.

This article thus introduces the PDF. Given specific motor geometries and material properties, the PDF *describes the flux distribution pattern on designated boundaries of the motor under the excitation of one phase current.*

Fig. 6 illustrates the flux distribution of the studied six-phase SPM with the energized phase highlighted. Fig. 7 shows the slot numbering convention relative to the energized phase, as well as the definition of a series of local coordinates attached to stator teeth of the studied motor, where $h_0 = h_s - h_1$.

The PDF on the tooth edge is defined as follows:

$$\lambda(x) = \frac{B_n(x)}{N_s i/a} \tag{1}$$

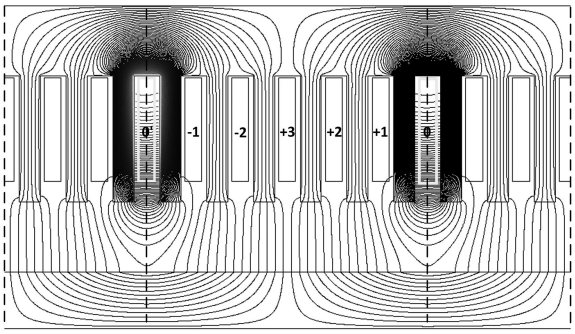

Fig. 6. Illustration of the flux distribution pattern with single-phase excitation (machine flattened for easier illustration).

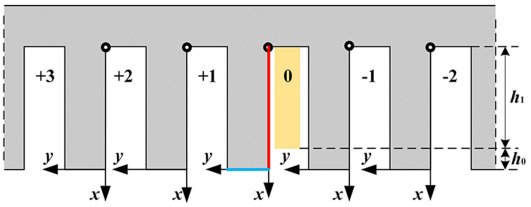

Fig. 7. Relative slot numbering convention and coordinate definitions of the stator of the studied motor.

where i is the phase current, with a reference direction pointing out of this article; a is the number of parallel branches; N_s is the number of conductors per slot; and $N_s i/a$ is, therefore, the slot current. $B_n(x)$ is the distribution of magnetic flux normal to the specified tooth edge, with a reference direction pointing out of the stator iron core.

The PDF on the slot centerline is defined similarly to that in (1); the only difference is that $B_n(x)$ is now the distribution of magnetic flux normal to the slot center line, with a reference direction pointing left.

The PDF on the tooth top is defined as follows

$$\lambda(y) = \frac{B_n(y)}{N_s i/a} \tag{2}$$

where $B_n(y)$ is the distribution of magnetic flux normal to the specified tooth top.

Compared with the definition of permeance $\Lambda = \frac{\phi}{N_s i/a}$, a basic physical quantity in magnetic circuits, the denominator of the PDF is the same, but the numerator changes from the total flux ϕ to the flux distribution $B_n(x)$ and $B_n(y)$. Therefore, the PDF is a physical quantity that describes the flux distribution normal to the analyzed boundaries, with the unit of $\mathrm{Wb} \times \mathrm{A}^{-1} \times \mathrm{m}^{-2}$.

The PDF is an essential parameter that reflects the characteristic of the motor magnetic circuit. When the magnetic circuit of the motor is linear, the PDF does not vary with the excitation current.

B. Denotation Custom

To differentiate PDFs on different stator boundaries, a proper denotation custom is needed. Denotation of PDFs involves two subscripts and one superscript in general, shown as follows:

$$\lambda_{e,l}^{+k}(\cdot). \tag{3}$$

The superscript indicates the location of the stator boundary measured by the relative slot number it belongs to. For example, a superscript of "0" indicates the boundary belongs to the slot numbering "0" in Fig. 7, i.e., the slot with active current excitation. A superscript of "+1" indicates the boundary belongs to the slot numbering "+1" in Fig. 7. For the studied six-phase concentrated-winding SPM, possible values of the superscript are -2, -1, 0, $+1$, $+2$, and $+3$.

The first subscript indicates the type of boundary. It is denoted as "e" for the tooth edge, "t" for the tooth top, and "sc" for the slot centerline.

The second subscript indicates whether the boundary is on the left or right of the affiliated slot. It is denoted as "*l*" if the boundary is on the left of the slot and "*r*" if on the right. The second subscript does not apply to the slot centerline and is omitted in that case.

It should be noted that the tooth-top PDFs can always be expressed in two ways using this denotation custom. For example, the PDF of the blue line in Fig. 7 can either be denoted as $\lambda_{t,l}^{+0}(y)$ or $\lambda_{t,r}^{+1}(y)$. Denotations of tooth edges and slot centerlines, however, are unique.

C. Properties of PDFs

As can be seen from Fig. 6, the flux distributions excited by a single -phase current possess many spatial symmetries, which can be exploited to reduce the number of PDFs needed to characterize the stator flux distribution.

1) The flux distributions on stator tooth edges are mirror symmetrical about the centerline of the excitation source, which leads to the following properties of PDFs:

$$\lambda_{e,l}^{+k}(x) = -\lambda_{e,r}^{-k}(x) \quad k = 0,1,2,3 \tag{4}$$

$$\lambda_{e,r}^{+k}(x) = -\lambda_{e,l}^{-k}(x) \quad k = 0,1,2,3. \tag{5}$$

Note that the minus sign is introduced because the reference direction of PDFs is always pointing out of the stator core.

2) The flux distributions on stator tooth tops are mirror symmetrical about the centerline of the excitation source, which leads to the following properties of PDFs:

$$\lambda_{t,l}^{+k}(y) = -\lambda_{t,r}^{-k}(b_t - y) \quad k = 0,1,2 \tag{6}$$

where b_t stands for the tooth width.

To simplify denotations, define

$$\lambda_{t,r}^{-k}(b_t - y) \underline{\underline{\mathrm{def}}} \lambda_{t,r}^{-k}(y)'. \tag{7}$$

Then, (6) simplifies to

$$\lambda_{t,l}^{+k}(y) = -\lambda_{t,r}^{-k}(y)' \; k = 0,1,2 \tag{8}$$

which is very similar to (4) in form.

3) For slot edges that are far away from the excitation source, their flux distributions are approximately identical.

This is because all slot edges far from the excitation source have the same magnetic potentials. Moreover, their position

TABLE II
INDEPENDENT PDFS OF THE STUDIED MOTOR

Types of stator boundaries	Independent permeance distribution functions
Tooth edge	$\lambda^{0}_{e,l}(x)$, $\lambda^{+1}_{e,r}(x)$, $\lambda^{+1}_{e,l}(x)$, $\lambda^{+2}_{e,l}(x)$,
Tooth top	$\lambda^{+0}_{t,l}(y)$, $\lambda^{+1}_{t,l}(y)$, $\lambda^{+2}_{t,l}(y)$,
Slot centerline	$\lambda^{0}_{sc}(x)$

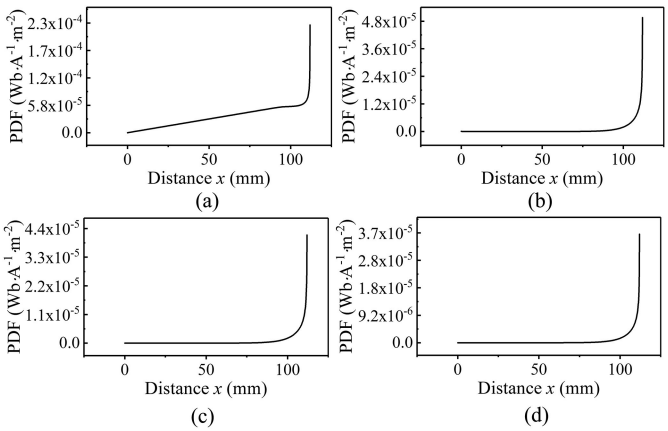

Fig. 8. Tooth-edge PDFs extracted by magnetostatic finite-element simulation. (a) $\lambda^{0}_{e,l}(x)$. (b) $\lambda^{+1}_{e,r}(x)$. (c) $\lambda^{+1}_{e,l}(x)$. (d) $\lambda^{+2}_{e,l}(x)$.

relative to the nonsalient rotor is also identical. Therefore, the resulting flux distribution is identical.

For slot edges that are close to the excitation source, however, they are caught in the leakage flux path of the excited phase. Therefore, the flux distribution is no longer the same as the ones farther away from the excitation source.

How "far" is enough really depends on the slot-opening-to-airgap-length ratio. The slot leakage flux tends to spread less to adjacent slots if the slot-opening-to-airgap-length ratio is larger. For the studied motor, it is found the flux distributions of slot edges become essentially identical if they are apart from the excitation source by one slot, which leads to the following properties of PDFs:

$$\lambda^{\pm 2}_{e,l}(x) \approx \lambda^{\pm 2}_{e,r}(x) \approx \lambda^{\pm 3}_{e,l}(x) \approx \lambda^{\pm 3}_{e,r}(x). \tag{9}$$

4) For those slots without active current excitations, the flux distributions on slot centerlines are negligible compared with that in the slot with active current excitation, which leads to the following properties of PDFs:

$$\lambda^{\pm k}_{\mathrm{sc}}(x) \approx 0 \quad k = 1, 2, 3. \tag{10}$$

For the single-pole model of the machine shown in Fig. 7, there are a total of 12 tooth edges, 6 tooth tops, and 6 slot centerlines, which correspond to a total of 24 PDFs. Using the four properties mentioned above, the number of independent PDFs can be reduced to four for the tooth edges, three for the tooth tops, and one for the slot centerlines, which are summarized in Table II.

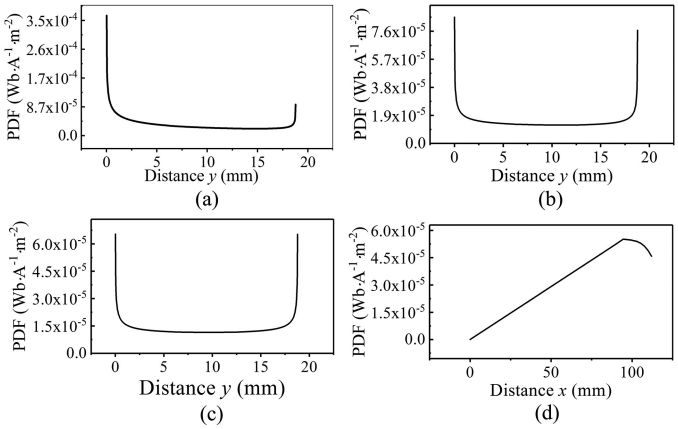

Fig. 9. Tooth-top and slot-centerline PDFs extracted by magnetostatic finite-element simulation. (a) $\lambda^{+0}_{t,l}(y)$. (b) $\lambda^{+1}_{t,l}(y)$. (c) $\lambda^{+2}_{t,l}(y)$. (d) $\lambda^{0}_{\mathrm{sc}}(y)$.

D. Finite-Element Extraction of PDFs

The aforementioned eight independent PDFs can all be extracted by the finite-element model of the studied SPM with a single simulation run. Extracted PDFs are shown in Figs. 8 and 9.

To facilitate numerical manipulations, each PDF is mathematically represented as a column vector. The dimension of the vector is determined by the spatial resolution needed to characterize the EM force on the stator boundaries.

E. Relations to Inductance Matrix

The general form of the inductance matrix of a six-phase motor is shown as follows

$$L = \begin{bmatrix} L_{11} & L_{12} & L_{13} & L_{14} & L_{15} & L_{16} \\ L_{21} & L_{22} & L_{23} & L_{24} & L_{25} & L_{26} \\ L_{31} & L_{32} & L_{33} & L_{34} & L_{35} & L_{36} \\ L_{41} & L_{42} & L_{43} & L_{44} & L_{45} & L_{46} \\ L_{51} & L_{52} & L_{53} & L_{54} & L_{55} & L_{56} \\ L_{61} & L_{62} & L_{63} & L_{64} & L_{65} & L_{66} \end{bmatrix}. \tag{11}$$

Due to the rotational symmetry of the stator core and stator windings of the studied motor, the inductance matrix only has six independent elements, L_{11}, L_{21}, L_{31}, L_{41}, L_{51}, and L_{61}. By integrating the PDFs along corresponding stator boundaries and calculating mutual flux linkages between different phases, all six inductances can be analytically expressed by PDFs as follows:

$$\begin{aligned} L_{11} = \frac{2P \cdot N_s^2 \cdot l_{ef}}{a^2} \Bigg[& \int_0^{h_1} \lambda^{0}_{e,l} \frac{x}{h_1} dx + \int_{h_1}^{h_1+h_0} \lambda^{0}_{e,l} dx \\ & + \int_0^{h_1+h_0} \left(\lambda^{+1}_{e,r} + \lambda^{+1}_{e,l} + 3\lambda^{+2}_{e,l} \right) dx \\ & + \int_0^{b_t} \left(\lambda^{0}_{t,l} + \lambda^{+1}_{t,l} + \lambda^{+2}_{t,l} \right) dy \Bigg] \end{aligned} \tag{12}$$

TABLE III
COMPARISON OF INDUCTANCE CALCULATION RESULTS

	FEA	PDF	error
L_{11} (mH)	2.7345	2.8079	2.68%
L_{21} (mH)	0.5255	0.5395	2.64%
L_{31} (mH)	0.2483	0.2555	2.90%
L_{41} (mH)	0.0002	0	-
L_{51} (mH)	-0.2479	-0.2555	3.06%
L_{61} (mH)	-0.5254	-0.5395	2.68%

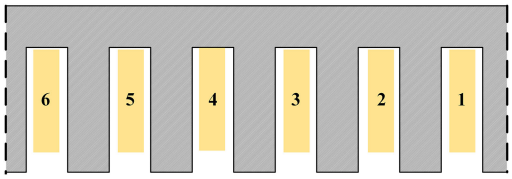

Fig. 10. Absolute slot and phase numbering convention of the studied motor.

$$L_{21} = \frac{2P \cdot N_s^2 \cdot l_{ef}}{a^2} \left[\int_0^{h_1+h_0} \left(\lambda_{e,l}^{+1} + 3\lambda_{e,l}^{+2} \right) dx + \int_0^{b_t} \left(\lambda_{t,l}^{+1} + \lambda_{t,l}^{+2} \right) dy \right] \tag{13}$$

$$L_{31} = \frac{2P \cdot N_s^2 \cdot l_{ef}}{a^2} \left(\int_0^{h_1+h_0} 2\lambda_{e,l}^{+2} dx + \int_0^{b_t} \lambda_{t,l}^{+2} dy \right) \tag{14}$$

$$L_{41} = 0 \tag{15}$$

$$L_{51} = -L_{31} \tag{16}$$

$$L_{61} = -L_{21} \tag{17}$$

where l_{ef} is the effective stator core length.

The inductances calculated from the FEA and from the PDFs are compared in Table III. The errors are small, which confirms the precision of using PDFs to characterized machine magnetic field.

IV. STATOR FLUX DISTRIBUTION BY ARMATURE CURRENTS

To calculate the flux distribution on stator boundaries by armature currents, the basic idea is to first calculate the flux distribution induced by each phase current and then superpose the results from all six phases together to obtain the combined flux distribution.

In Section III-B, PDFs are denoted relative to the slot with active current excitation. To describe the superposition process mathematically, however, an absolute slot and phase numbering convention needs to be introduced, as shown in Fig. 10

In Fig. 10, all slots and phases are numbered sequentially from 1 to 6. Slot edges are numbered after the slot they belong to, and tooth tops are numbered after the slot to its right. For example, the left and right edges of slot number "*m*" are denoted in subscript as "*m, l*" and "*m, r*" respectively, and the tooth top to the left of slot number "*m*" is denoted in subscript as "*m, t*".

The superposition process can be expressed in very succinct matrix forms. The flux distributions on tooth tops are

$$\begin{bmatrix} B_{1,t}^a(y,t) \\ B_{2,t}^a(y,t) \\ B_{3,t}^a(y,t) \\ B_{4,t}^a(y,t) \\ B_{5,t}^a(y,t) \\ B_{6,t}^a(y,t) \end{bmatrix} = \frac{N_s}{a} \begin{bmatrix} \lambda_{t,l}^0 & \lambda_{t,r}^0 & \lambda_{t,r}^{-1} & \lambda_{t,r}^{-2} & -\lambda_{t,l}^{+2} & -\lambda_{t,l}^{+1} \\ \lambda_{t,l}^{+1} & \lambda_{t,l}^0 & \lambda_{t,r}^0 & \lambda_{t,r}^{-1} & \lambda_{t,r}^{-2} & -\lambda_{t,l}^{+2} \\ \lambda_{t,l}^{+2} & \lambda_{t,l}^{+1} & \lambda_{t,l}^0 & \lambda_{t,r}^0 & \lambda_{t,r}^{-1} & \lambda_{t,r}^{-2} \\ -\lambda_{t,r}^{-2} & \lambda_{t,l}^{+2} & \lambda_{t,l}^{+1} & \lambda_{t,l}^0 & \lambda_{t,r}^0 & \lambda_{t,r}^{-1} \\ -\lambda_{t,r}^{-1} & -\lambda_{t,r}^{-2} & \lambda_{t,l}^{+2} & \lambda_{t,l}^{+1} & \lambda_{t,l}^0 & \lambda_{t,r}^0 \\ -\lambda_{t,r}^0 & -\lambda_{t,r}^{-1} & -\lambda_{t,r}^{-2} & \lambda_{t,l}^{+2} & \lambda_{t,l}^{+1} & \lambda_{t,l}^0 \end{bmatrix} \begin{bmatrix} i_1(t) \\ i_2(t) \\ i_3(t) \\ i_4(t) \\ i_5(t) \\ i_6(t) \end{bmatrix} \tag{18}$$

where phase current $i_1(t)$ is a $1 \times N$ row vector, with different columns representing currents at different time instants; each PDF is $M_1 \times 1$ column vector; and $B_{1t}^a(y,t)$ is an $M_1 \times N$ matrix, with rows representing different spatial positions and columns representing different time instants.

Utilizing the properties of PDFs discussed in Section III-C, (18) can be represented by only three independent PDFs of the tooth tops as

$$\begin{bmatrix} B_{1,t}^a(y,t) \\ B_{2,t}^a(y,t) \\ B_{3,t}^a(y,t) \\ B_{4,t}^a(y,t) \\ B_{5,t}^a(y,t) \\ B_{6,t}^a(y,t) \end{bmatrix} = \frac{N_s}{a} \begin{bmatrix} \lambda_{t,l}^0 & -\lambda_{t,l}^{0'} & -\lambda_{t,l}^{+1'} & -\lambda_{t,l}^{+2'} & -\lambda_{t,l}^{+2} & -\lambda_{t,l}^{+1} \\ \lambda_{t,l}^{+1} & \lambda_{t,l}^0 & -\lambda_{t,l}^{0'} & -\lambda_{t,l}^{+1'} & -\lambda_{t,l}^{+2'} & -\lambda_{t,l}^{+2} \\ \lambda_{t,l}^{+2} & \lambda_{t,l}^{+1} & \lambda_{t,l}^0 & -\lambda_{t,l}^{0'} & -\lambda_{t,l}^{+1'} & -\lambda_{t,l}^{+2'} \\ \lambda_{t,l}^{+2'} & \lambda_{t,l}^{+2} & \lambda_{t,l}^{+1} & \lambda_{t,l}^0 & -\lambda_{t,l}^{0'} & -\lambda_{t,l}^{+1'} \\ \lambda_{t,l}^{+1'} & \lambda_{t,l}^{+2'} & \lambda_{t,l}^{+2} & \lambda_{t,l}^{+1} & \lambda_{t,l}^0 & -\lambda_{t,l}^{0'} \\ \lambda_{t,l}^{0'} & \lambda_{t,l}^{+1'} & \lambda_{t,l}^{+2'} & \lambda_{t,l}^{+2} & \lambda_{t,l}^{+1} & \lambda_{t,l}^0 \end{bmatrix} \begin{bmatrix} i_1(t) \\ i_2(t) \\ i_3(t) \\ i_4(t) \\ i_5(t) \\ i_6(t) \end{bmatrix} . \tag{19}$$

The superposed flux distributions on left and right slot edges are

$$\begin{bmatrix} B_{1,l}^a(x,t) \\ B_{2,l}^a(x,t) \\ B_{3,l}^a(x,t) \\ B_{4,l}^a(x,t) \\ B_{5,l}^a(x,t) \\ B_{6,l}^a(x,t) \end{bmatrix} = \frac{N_s}{a} \begin{bmatrix} \lambda_{e,l}^0 \lambda_{e,l}^{-1} & \lambda_{e,l}^{-2} & \lambda_{e,l}^{-3} & -\lambda_{e,l}^{+2} & -\lambda_{e,l}^{+1} \\ \lambda_{e,l}^{+1} & \lambda_{e,l}^0 & \lambda_{e,l}^{-1} & \lambda_{e,l}^{-2} & \lambda_{e,l}^{-3} & -\lambda_{e,l}^{+2} \\ \lambda_{e,l}^{+2} & \lambda_{e,l}^{+1} & \lambda_{e,l}^0 & \lambda_{e,l}^{-1} & \lambda_{e,l}^{-2} & \lambda_{e,l}^{-3} \\ \lambda_{e,l}^{+3} & \lambda_{e,l}^{+2} & \lambda_{e,l}^{+1} & \lambda_{e,l}^0 & \lambda_{e,l}^{-1} & \lambda_{e,l}^{-2} \\ -\lambda_{e,l}^{-2} & \lambda_{e,l}^{+3} & \lambda_{e,l}^{+2} & \lambda_{e,l}^{+1} & \lambda_{e,l}^0 & \lambda_{e,l}^{-1} \\ -\lambda_{e,l}^{-1} & -\lambda_{e,l}^{-2} \lambda_{e,l}^{+3} & \lambda_{e,l}^{+2} & \lambda_{e,l}^{+1} & \lambda_{e,l}^0 \end{bmatrix} \begin{bmatrix} i_1(t) \\ i_2(t) \\ i_3(t) \\ i_4(t) \\ i_5(t) \\ i_6(t) \end{bmatrix} \tag{20}$$

$$\begin{bmatrix} B_{1,r}^a(x,t) \\ B_{2,r}^a(x,t) \\ B_{3,r}^a(x,t) \\ B_{4,r}^a(x,t) \\ B_{5,r}^a(x,t) \\ B_{6,r}^a(x,t) \end{bmatrix} = \frac{N_s}{a} \begin{bmatrix} \lambda_{e,r}^0 & \lambda_{e,r}^{-1} & \lambda_{e,r}^{-2} \lambda_{e,r}^{-3} & -\lambda_{e,r}^{+2} & -\lambda_{e,r}^{+1} \\ \lambda_{e,r}^{+1} & \lambda_{e,r}^0 & \lambda_{e,r}^{-1} \lambda_{e,r}^{-2} & \lambda_{e,r}^{-3} & -\lambda_{e,r}^{+2} \\ \lambda_{e,r}^{+2} & \lambda_{e,r}^{+1} & \lambda_{e,r}^0 \lambda_{e,r}^{-1} & \lambda_{e,r}^{-2} & \lambda_{e,r}^{-3} \\ \lambda_{e,r}^{+3} & \lambda_{e,r}^{+2} & \lambda_{e,r}^{+1} \lambda_{e,r}^0 & \lambda_{e,r}^{-1} & \lambda_{e,r}^{-2} \\ -\lambda_{e,r}^{-2} & \lambda_{e,r}^{+3} & \lambda_{e,r}^{+2} \lambda_{e,r}^{+1} & \lambda_{e,r}^0 & \lambda_{e,r}^{-1} \\ -\lambda_{e,r}^{-1} & -\lambda_{e,r}^{-2} & \lambda_{e,r}^{+3} \lambda_{e,r}^{+2} & \lambda_{e,r}^{+1} & \lambda_{e,r}^0 \end{bmatrix} \begin{bmatrix} i_1(t) \\ i_2(t) \\ i_3(t) \\ i_4(t) \\ i_5(t) \\ i_6(t) \end{bmatrix} . \tag{21}$$

Utilizing the properties of PDFs discussed in Section III-C, (20) and (21) can be represented by the four independent PDFs

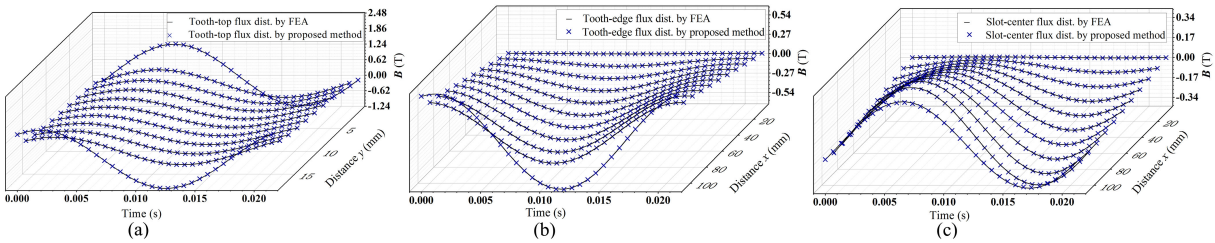

Fig. 11. Comparison of armature-current-induced flux distribution on specified stator boundaries. (a) Tooth top "3, *t*." (b) Tooth edge "4, *r*." (c) Slot centerline "2."

of the slot edges as

$$\begin{bmatrix} B^a_{1,l}(x,t) \\ B^a_{2,l}(x,t) \\ B^a_{3,l}(x,t) \\ B^a_{4,l}(x,t) \\ B^a_{5,l}(x,t) \\ B^a_{6,l}(x,t) \end{bmatrix} = \frac{N_s}{a} \begin{bmatrix} \lambda^0_{e,l} & -\lambda^{+1}_{e,r} & -\lambda^{+2}_{e,l} & -\lambda^{+2}_{e,l} & -\lambda^{+2}_{e,l} & -\lambda^{+1}_{e,l} \\ \lambda^{+1}_{e,l} & \lambda^0_{e,l} & -\lambda^{+1}_{e,r} & -\lambda^{+2}_{e,l} & -\lambda^{+2}_{e,l} & -\lambda^{+2}_{e,l} \\ \lambda^{+2}_{e,l} & \lambda^{+1}_{e,l} & \lambda^0_{e,l} & -\lambda^{+1}_{e,r} & -\lambda^{+2}_{e,l} & -\lambda^{+2}_{e,l} \\ \lambda^{+2}_{e,l} & \lambda^{+2}_{e,l} & \lambda^{+1}_{e,l} & \lambda^0_{e,l} & -\lambda^{+1}_{e,r} & -\lambda^{+2}_{e,l} \\ \lambda^{+2}_{e,l} & \lambda^{+2}_{e,l} & \lambda^{+2}_{e,l} & \lambda^{+1}_{e,l} & \lambda^0_{e,l} & -\lambda^{+1}_{e,r} \\ \lambda^{+1}_{e,r} & \lambda^{+2}_{e,l} & \lambda^{+2}_{e,l} & \lambda^{+2}_{e,l} & \lambda^{+1}_{e,l} & \lambda^0_{e,l} \end{bmatrix} \begin{bmatrix} i_1(t) \\ i_2(t) \\ i_3(t) \\ i_4(t) \\ i_5(t) \\ i_6(t) \end{bmatrix} \tag{22}$$

$$\begin{bmatrix} B^a_{1,r}(x,t) \\ B^a_{2,r}(x,t) \\ B^a_{3,r}(x,t) \\ B^a_{4,r}(x,t) \\ B^a_{5,r}(x,t) \\ B^a_{6,r}(x,t) \end{bmatrix} = \frac{N_s}{a} \begin{bmatrix} -\lambda^0_{e,l} & -\lambda^{+1}_{e,l} & -\lambda^{+2}_{e,l} & -\lambda^{+2}_{e,l} & -\lambda^{+2}_{e,l} & -\lambda^{+1}_{e,r} \\ \lambda^{+1}_{e,r} & -\lambda^0_{e,l} & -\lambda^{+1}_{e,l} & -\lambda^{+2}_{e,l} & -\lambda^{+2}_{e,l} & -\lambda^{+2}_{e,l} \\ \lambda^{+2}_{e,l} & \lambda^{+1}_{e,r} & -\lambda^0_{e,l} & -\lambda^{+1}_{e,l} & -\lambda^{+2}_{e,l} & -\lambda^{+2}_{e,l} \\ \lambda^{+2}_{e,l} & \lambda^{+2}_{e,l} & \lambda^{+1}_{e,r} & -\lambda^0_{e,l} & -\lambda^{+1}_{e,l} & -\lambda^{+2}_{e,l} \\ \lambda^{+2}_{e,l} & \lambda^{+2}_{e,l} & \lambda^{+2}_{e,l} & \lambda^{+1}_{e,r} & -\lambda^0_{e,l} & -\lambda^{+1}_{e,l} \\ \lambda^{+1}_{e,l} & \lambda^{+2}_{e,l} & \lambda^{+2}_{e,l} & \lambda^{+2}_{e,l} & \lambda^{+1}_{e,r} & -\lambda^0_{e,l} \end{bmatrix} \begin{bmatrix} i_1(t) \\ i_2(t) \\ i_3(t) \\ i_4(t) \\ i_5(t) \\ i_6(t) \end{bmatrix}. \tag{23}$$

The flux distributions on the centerlines for slot *m* are

$$B^a_{m,\mathrm{sc}}(x,t) = \frac{N_s}{a} \cdot \lambda^0_{\mathrm{sc}}(x)\, i_m(t), \quad m = 1,2,\ldots,6. \tag{24}$$

Fig. 11 compares the armature-current-induced flux distributions calculated by FEA and the proposed method under rated condition. Flux distributions on tooth top "3, *t*," slot edge "4, *r*," and slot centerline "2" given by the two methods agree very closely across the specified boundaries over the entire fundamental cycle.

V. Stator Flux Distribution by PMs

To calculate the flux distribution along stator boundaries induced by rotating PMs, the following solution process was proposed, as shown in Fig. 12.

A. PM-Induced Flux Distribution Along Slotless Stator Bore

The flux distribution along the slotless stator bore reflects the inherent excitation characteristics of the PM rotor. Fig. 13 shows the rotor-synchronous angular coordinate system of the motor, whose origin is anchored on the *d*-axis of the PM rotor.

In the rotor-synchronous coordinate system, the radial flux distribution induced by the PM rotor along the slotless stator bore is time independent and can be expressed in the following

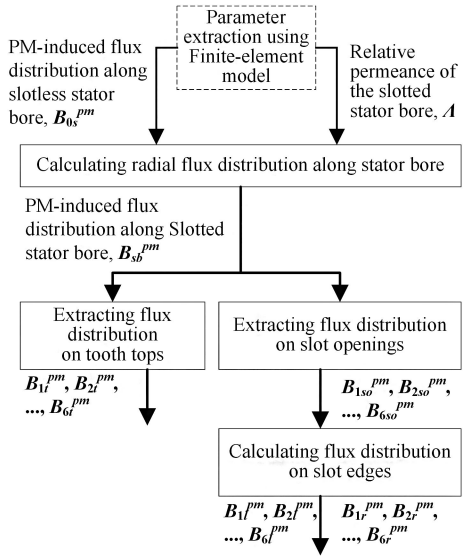

Fig. 12. Overall process for calculating stator flux distribution induced by PMs.

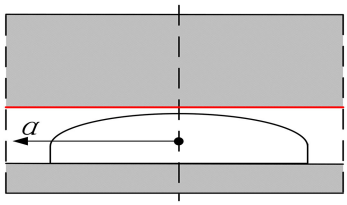

Fig. 13. Rotor-synchronous angular coordinate system of the motor.

series form:

$$B^{\mathrm{pm}}_{0r}(\alpha) = \sum_{n=1}^{\infty} B_n \cos(n\alpha + \varphi_n) \tag{25}$$

where B_n is the magnitude of the *n*th order flux harmonics, and φ_n is the phase angle of the *n*th order flux harmonics, both of which can be extracted by a slotless finite-element model.

Fig. 14 shows the stationary angular coordinate system of the motor, whose origin is anchored on the axis of phase-1 winding. Defining the rotor angle $\theta_r(t)$ to be the angle from phase-1 axis to the rotor *d*-axis, then for any angle θ in the stationary coordinate system, its corresponding angle in the rotor-synchronous coordinate system is

$$\alpha = \theta - \theta_r(t). \tag{26}$$

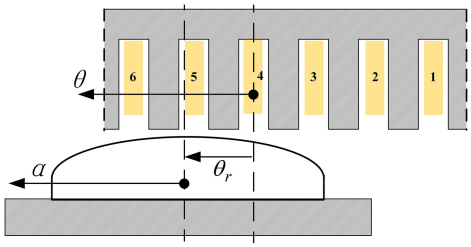

Fig. 14. Stationary angular coordinate system of the motor.

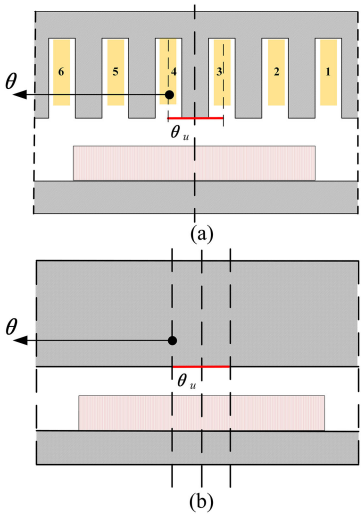

Fig. 15. Extraction of relative permeance of the slotting effect. (a) Finite-element model with stator slots. (b) Finite-element model without stator slots.

Substituting (26) into (25), the PM-induced radial flux distribution along slotless stator bore in the stationary angular coordinate system can be expressed as

$$B_{0s}^{\mathrm{pm}}(\theta,t)=\sum_{n=1}^{\infty}B_n\cos\left(n\left(\theta-\theta_r\left(t\right)\right)+\varphi_n\right). \tag{27}$$

B. Relative Permeance Along the Slotted Stator Bore

While the PM-induced flux distribution is rotating in space, the slotting effect is stationary and can be characterized by the relative permeance of the slotted stator bore. Fig. 15 shows the slotted and slotless motor models with a segment of stator bore highlighted. Dividing the radial flux distribution of the slotted model by that of the slotless model, the relative permeance along the highlighted section of the stator bore can be determined as

$$\Lambda\left(\theta\right)=B_{\mathrm{slot}}\left(\theta\right)/B_{\mathrm{slotless}}\left(\theta\right)\quad\theta\in\left[-\theta_u,0\right] \tag{28}$$

where θ_u is the slot pitch angle in electric degrees.

Due to the rotational symmetry of the stator core, there is

$$\Lambda\left(\theta\right)=\Lambda\left(\theta+\theta_u\right). \tag{29}$$

The relative permeance along the slotted stator bore can thus be extended to the entire pole pitch, as shown in Fig. 16.

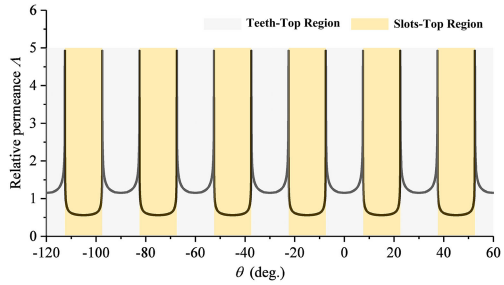

Fig. 16. Relative permeance of the slotted stator bore across one pole.

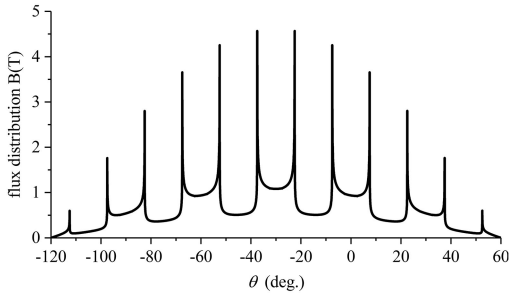

Fig. 17. PM-induced radial flux distribution along the stator bore of the studied motor across one pole.

The PM-induced radial flux distribution along the stator bore can therefore be obtained by multiplying $B_{0s}^{\mathrm{pm}}(\theta)$ and $\Lambda(\theta)$

$$B_{\mathrm{sb}}^{\mathrm{pm}}\left(\theta,t\right)=\Lambda\left(\theta\right)\cdot\sum_{n=1}^{\infty}B_n\cos\left(n\left(\theta-\theta_r\left(t\right)\right)+\varphi_n\right). \tag{30}$$

The calculation result for the studied motor when $\theta_r(t)=-30^\circ$ is given in Fig. 17.

C. PM-Induced Flux Distribution at Stator Tooth Tops

The PM-induced flux distribution at stator tooth tops can be directly sampled from corresponding sections of $B_{\mathrm{sb}}^{\mathrm{pm}}$ by

$$\begin{bmatrix}B_{1,t}^{\mathrm{pm}}\left(y,t\right)\\B_{2,t}^{\mathrm{pm}}\left(y,t\right)\\B_{3,t}^{\mathrm{pm}}\left(y,t\right)\\B_{4,t}^{\mathrm{pm}}\left(y,t\right)\\B_{5,t}^{\mathrm{pm}}\left(y,t\right)\\B_{6,t}^{\mathrm{pm}}\left(y,t\right)\end{bmatrix}=\begin{bmatrix}B_{\mathrm{sb}}^{\mathrm{pm}}\left(\theta,t\right),&\theta\epsilon\left[-3\theta_u+\frac{1}{2}\theta_{\mathrm{so}},-2\theta_u-\frac{1}{2}\theta_{\mathrm{so}}\right]\\B_{\mathrm{sb}}^{\mathrm{pm}}\left(\theta,t\right),&\theta\epsilon\left[-2\theta_u+\frac{1}{2}\theta_{\mathrm{so}},-\theta_u-\frac{1}{2}\theta_{\mathrm{so}}\right]\\B_{\mathrm{sb}}^{\mathrm{pm}}\left(\theta,t\right),&\theta\epsilon\left[-\theta_u+\frac{1}{2}\theta_{\mathrm{so}},-\frac{1}{2}\theta_{\mathrm{so}}\right]\\B_{\mathrm{sb}}^{\mathrm{pm}}\left(\theta,t\right),&\theta\epsilon\left[\frac{1}{2}\theta_{\mathrm{so}},\theta_u-\frac{1}{2}\theta_{\mathrm{so}}\right]\\B_{\mathrm{sb}}^{\mathrm{pm}}\left(\theta,t\right),&\theta\epsilon\left[\theta_u+\frac{1}{2}\theta_{\mathrm{so}},2\theta_u-\frac{1}{2}\theta_{\mathrm{so}}\right]\\B_{\mathrm{sb}}^{\mathrm{pm}}\left(\theta,t\right),&\theta\epsilon\left[2\theta_u+\frac{1}{2}\theta_{\mathrm{so}},3\theta_u-\frac{1}{2}\theta_{\mathrm{so}}\right]\end{bmatrix} \tag{31}$$

where θ_{so} is the slot opening pitch angle in electric degrees.

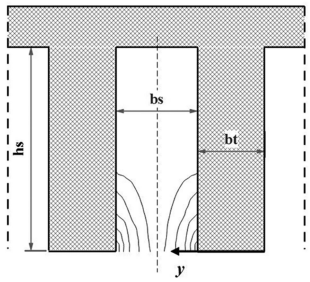

Fig. 18. Illustration of flux lines in stator slots with only PM excitation.

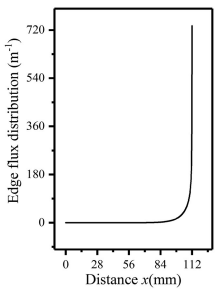

Fig. 19. Normalized slot-edge flux dist. pattern with only PM excitation.

D. PM-Induced Flux Distribution at Slot Edges

The PM-induced flux distribution at stator slot openings can be directly sampled from corresponding sections of $B_{\mathrm{sb}}^{\mathrm{pm}}$ by

$$\begin{bmatrix} B_{1,\mathrm{so}}^{\mathrm{pm}}(y,t) \\ B_{2,\mathrm{so}}^{\mathrm{pm}}(y,t) \\ B_{3,\mathrm{so}}^{\mathrm{pm}}(y,t) \\ B_{4,\mathrm{so}}^{\mathrm{pm}}(y,t) \\ B_{5,\mathrm{so}}^{\mathrm{pm}}(y,t) \\ B_{6,\mathrm{so}}^{\mathrm{pm}}(y,t) \end{bmatrix} = \begin{bmatrix} B_{\mathrm{sb}}^{\mathrm{pm}}(\theta,t), & \theta\epsilon\left[-3\theta_u - \frac{1}{2}\theta_{\mathrm{so}}, -3\theta_u + \frac{1}{2}\theta_{\mathrm{so}}\right] \\ B_{\mathrm{sb}}^{\mathrm{pm}}(\theta,t), & \theta\epsilon\left[-2\theta_u - \frac{1}{2}\theta_{\mathrm{so}}, -2\theta_u + \frac{1}{2}\theta_{\mathrm{so}}\right] \\ B_{\mathrm{sb}}^{\mathrm{pm}}(\theta,t), & \theta\epsilon\left[-\theta_u - \frac{1}{2}\theta_{\mathrm{so}}, -\theta_u + \frac{1}{2}\theta_{\mathrm{so}}\right] \\ B_{\mathrm{sb}}^{\mathrm{pm}}(\theta,t), & \theta\epsilon\left[-\frac{1}{2}\theta_{\mathrm{so}}, +\frac{1}{2}\theta_{\mathrm{so}}\right] \\ B_{\mathrm{sb}}^{\mathrm{pm}}(\theta,t), & \theta\epsilon\left[\theta_u - \frac{1}{2}\theta_{\mathrm{so}}, \theta_u + \frac{1}{2}\theta_{\mathrm{so}}\right] \\ B_{\mathrm{sb}}^{\mathrm{pm}}(\theta,t), & \theta\epsilon\left[2\theta_u - \frac{1}{2}\theta_{\mathrm{so}}, 2\theta_u + \frac{1}{2}\theta_{\mathrm{so}}\right] \end{bmatrix}. \tag{32}$$

With only PM excitations, the typical flux distribution in the stator slot is illustrated in Fig. 18. According to flux continuity theorem, magnetic fluxes that enter the slot opening should equal to fluxes that exit both edges of the slot.

Assuming the flux distribution pattern of the slot edge is $p(x)$, which is normalized to $\int_0^{h_s} p(x)dx = 1$. For linear magnetic circuits, $p(x)$ is generally a fixed function that can be extracted by FEA, as shown in Fig. 19.

The total flux (per unit axial length) that enters the left half and right half of slot opening "*m*" can be expressed as

$$\Phi_{m,l}(t) = \int_{b_t+b_s/2}^{b_t+b_s} B_{m,\mathrm{so}}^{\mathrm{pm}}(y,t)\,dy,\ m = 1,2,\ldots,6 \tag{33}$$

$$\Phi_{m,r}(t) = \int_{b_t}^{b_t+b_s/2} B_{m,\mathrm{so}}^{\mathrm{pm}}(y,t)\,dy,\ m = 1,2,\ldots,6. \tag{34}$$

Assuming that the flux that enters via the left half of the slot opening eventually goes to the left slot edge, and the flux that enters via the right half of the slot opening goes to the right slot edge. Then, at any time instant, the flux distribution along the left and right edges of slot "*m*" can be expressed as

$$B_{m,l}^{\mathrm{pm}}(x,t) = \Phi_{m,l}(t)\cdot p(x),\quad m = 1,2,\ldots,6 \tag{35}$$

$$B_{m,r}^{\mathrm{pm}}(x,t) = \Phi_{m,r}(t)\cdot p(x),\quad m = 1,2,\ldots,6. \tag{36}$$

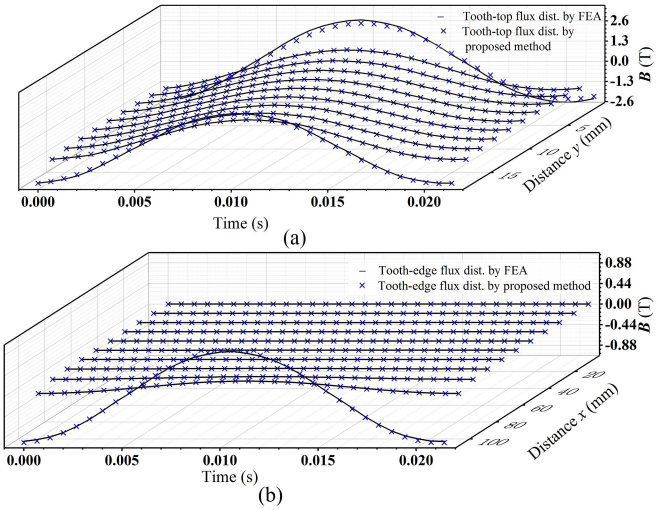

Fig. 20. Comparison of PM-induced flux distribution on stator boundaries. (a) Tooth top "3, *t*." (b) Tooth edge "4, *r*."

Fig. 20 compares the PM-induced flux distributions calculated by FEA and the proposed method on tooth top "3, *t*" and slot edge "4, *r*", respectively. Flux distributions given by the two methods agree very closely across the specified boundaries over the entire fundamental cycle.

VI. Stator EM Force Distribution

A. Combined Flux Distribution on Stator Boundaries

In Section III, the armature-current-induced flux distributions along stator boundaries of the studied motor have been obtained in (19), (22), and (23). In Section IV, the PM-induced flux distributions along stator boundaries have been obtained in (31), (35), and (36). By superposing the flux distributions from these two excitation sources together, the actual flux distributions along stator boundaries of the motor can be finally obtained as

$$B_{m,t}(y,t) = B_{m,t}^{a}(y,t) + B_{m,t}^{\mathrm{pm}}(y,t),\quad m = 1,2,\ldots,6 \tag{37}$$

$$B_{m,l}(x,t) = B_{m,l}^{a}(x,t) + B_{m,l}^{\mathrm{pm}}(x,t),\quad m = 1,2,\ldots,6 \tag{38}$$

$$B_{m,r}(x,t) = B_{m,r}^{a}(x,t) + B_{m,r}^{\mathrm{pm}}(x,t),\quad m = 1,2,\ldots,6. \tag{39}$$

Fig. 21 compares the flux distributions simultaneously induced by armature currents and PMs calculated by FEA and the proposed method, which agree very closely.

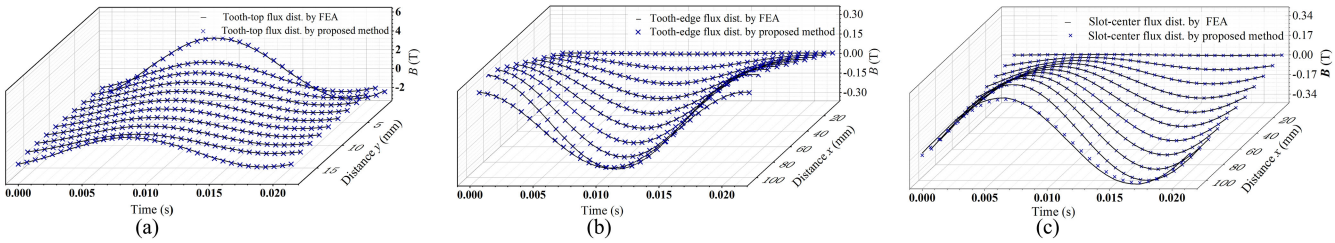

Fig. 21. Comparison of combined flux distribution on specified stator boundaries. (a) Tooth top "3, *t*." (b) Tooth edge "4, *r*." (c) Slot centerline "2."

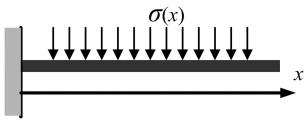

Fig. 22. Simplified cantilever beam model of stator teeth.

B. Radial Force on Stator Teeth

The EM force density on stator tooth tops can be determined according to the Maxwell stress tensor method as

$$\sigma_{m,t}(y,t) = \frac{B_{m,t}^2(y,t)}{2\mu_0}, \quad m = 1,2,\ldots,6. \tag{40}$$

Therefore, the radial force on stator tooth *m* can be calculated by integrating the stress along the tooth tops

$$F_{m,\text{radial}} = l_{ef}\int_0^{b_t}\sigma_{m,t}(y,t)\,dy = l_{ef}\int_0^{b_t}\frac{B_{m,t}^2(y,t)}{2\mu_0}dy. \tag{41}$$

C. Lateral Force on Stator Teeth

According to the absolute slot and tooth numbering convention in Fig. 10, the right edge of tooth "*m*" is the left edge of slot "*m*" and should be denoted as "*m*, *l*" accordingly. However, the left edge of stator tooth "*m*" is essentially the right edge of slot "$m+1$" and should be denoted as "$m+1$, *r*"

According to the basic symmetry of electric machines, $B_{7,r}(x,t) = -B_{1,r}(x,t)$. Then, for any stator tooth "*m,*" the EM force density on its left and right edges can be expressed uniformly as

$$\sigma_{m+1,r}(x,t) = \frac{B_{m+1,r}^2(x,t)}{2\mu_0}, \quad m = 1,2,\ldots,6 \tag{42}$$

$$\sigma_{m,l}(x,t) = \frac{B_{m,l}^2(x,t)}{2\mu_0}, \quad m = 1,2,\ldots,6. \tag{43}$$

If stator teeth are treated as cantilever beams, as shown in Fig. 22, the overall lateral force on stator tooth "*m*" is

$$F_{m,\text{lateral}} = l_{ef}\int_0^{h_s}\frac{B_{m+1,r}^2(x,t) - B_{m,l}^2(x,t)}{2\mu_0}dx. \tag{44}$$

The overall bending moment exerted on tooth *m* is

$$M_m = l_{ef}\int_0^{h_s} x\frac{B_{m+1,r}^2(x,t) - B_{m,l}^2(x,t)}{2\mu_0}dx. \tag{45}$$

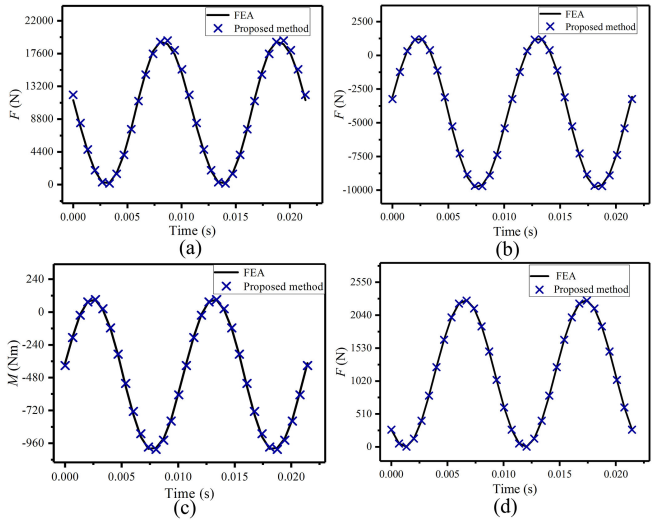

Fig. 23. Comparison of EM forces on stator tooth and stator coil given by FEA and the proposed method. (a) Radial force on tooth "3." (b) Lateral force on tooth "3." (c) Bending torque on tooth "3." (d) Radial force on coil "2."

D. Radial Force on Stator Coils

The force seen by the stator coil is primarily the Lorenz force of the slot current interacting with the slot leakage flux. For the coil in slot *m*, its Lorenz force can be calculated as

$$F_{m,\text{coil}} = \int_0^{h_1} B_{m,sc}^a(x,t)\left(\frac{N_s}{a}i_m(t)\frac{dx}{h_1}\right)l_{ef}. \tag{46}$$

Substituting (24) into (46) yields

$$\begin{aligned} F_{m,\text{coil}} &= \int_0^{h_1}\frac{N_s}{a}\lambda_{sc}^0(x)\,i_m(t)\,\frac{N_s i_m(t)}{ah_1}l_{ef}dx \\ &= \frac{N_s^2 i_m^2(t)\,l_{ef}}{a^2h_1}\int_0^{h_1}\lambda_{sc}^0(x)\,dx. \end{aligned} \tag{47}$$

E. Finite-Element Validation With Fundamental Currents

When the studied motor is fed by sinusoidal currents at rated condition, the radial force, lateral force, and bending moment on the stator tooth, as well as the radial force on the stator coil, are compared in Fig. 23, demonstrating very close agreement between results given by FEA and the proposed method.

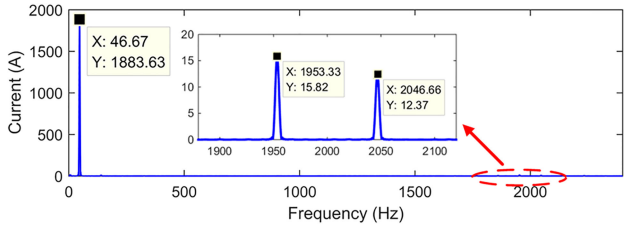

Fig. 24. Phase current spectrum.

TABLE IV
COMPARISON OF RADIAL EM FORCES ON STATOR TEETH

Frequency (Hz)		93.34		1906.70		2000.00		2093.33	
	Tooth #	FEA	PDF	FEA	PDF	FEA	PDF	FEA	PDF
Ampl-itude (N)	1	8971.7	9056.2	84.1	83.8	87.0	87.1	50.9	50.7
	2	8958.6	9117.2	49.0	49.3	79.8	80.5	76.1	76.4
	3	8957.2	9055.0	84.1	83.7	87.1	87.1	50.8	50.6
	4	8945.4	9122.3	48.9	49.3	79.6	80.6	75.9	76.4
	5	8947.8	9060.0	83.8	83.7	87.0	87.2	50.9	50.6
	6	9037.6	9120.6	49.6	49.3	80.6	80.5	76.9	76.5
Phase (deg.)	1	0.0	0.0	0.0	0.0	0.0	0.0	0.0	0.0
	2	-59.9	-59.8	-111.6	-111.9	198.5	198.4	129.2	129.0
	3	-121.4	-121.5	119.9	120.0	0.1	0.0	-121.3	-121.5
	4	178.7	180.2	8.5	8.2	198.5	198.4	9.2	9.0
	5	120.0	120.0	240.1	240.0	-1.4	0.0	118.2	118.5
	6	60.2	60.2	126.7	128.2	197.0	198.4	-110.7	-111.0

TABLE V
COMPARISON OF LATERAL EM FORCES ON STATOR TEETH

Frequency (Hz)		93.34		1906.70		2000.00		2093.33	
	Tooth #	FEA	PDF	FEA	PDF	FEA	PDF	FEA	PDF
Amplit-ude (N)	1	5311.5	5270.5	124.0	122.5	146.3	144.9	84.5	83.6
	2	5369.2	5381.7	86.2	85.7	141.9	141.2	114.4	113.9
	3	5462.7	5272.1	125.2	122.5	147.7	145.1	85.1	83.5
	4	5560.8	5409.2	87.3	86.2	144.1	142.6	116.3	114.6
	5	5439.2	5294.6	125.4	123.2	148.1	146.2	85.4	84.0
	6	5447.9	5382.2	86.9	85.7	143.0	141.2	115.6	114.0
Phase (deg.)	1	0.0	0.0	0.0	0.0	0.0	0.0	0.0	0.0
	2	300.2	300.1	-125.8	-125.8	-182.0	-182.0	-241.5	-241.4
	3	239.5	240.0	-240.1	-240.0	0.0	0.0	-119.8	-120.1
	4	178.0	178.2	-5.8	-5.5	-181.9	-182.0	-1.5	-1.6
	5	119.5	119.6	-120.0	-119.8	0.0	0.0	-240.1	-240.4
	6	59.9	60.0	-245.7	-245.8	-181.9	-182.0	-121.6	-121.4

F. Finite-Element Validation With Realistic Currents

To validate the proposed method in calculating stator EM forces induced by PWM harmonics, the six-phase PMSM along with its three-level neutral-point-clamped H-bridge inverter is implemented in PLECS. The PWM carriers have a fixed frequency of 1000 Hz and are phase shifted by 105° between two sets of three-phase windings. To achieve good sampling quality and sufficient spectrum resolution, the currents are sampled at 40 kHz for five fundamental cycles. The phase current spectrum near rated condition is shown in Fig. 24.

Tables IV–VII compare the major EM force harmonics given by FEA and the proposed method, including radial forces, lateral forces, and bending moments on stator teeth, as well as radial forces on stator coils.

As can be seen from the comparison, frequencies of harmonic components ($2f_e$, $2f_s$, $2f_s \pm 2f_e$) given by the two methods match exactly. Amplitudes and relative phase angles across all stator teeth and stator coils also agree closely.

TABLE VI
COMPARISON OF BENDING MOMENTS ON STATOR TEETH

Frequency (Hz)		93.34		1906.70		2000.00		2093.33	
	Tooth #	FEA	PDF	FEA	PDF	FEA	PDF	FEA	PDF
Ampli-tude (Nm)	1	530.4	526.9	10.8	10.6	12.5	12.4	7.2	7.1
	2	533.7	536.3	7.4	7.4	12.0	12.0	9.9	9.9
	3	547.5	527.0	10.9	10.6	12.7	12.4	7.3	7.1
	4	555.4	539.5	7.5	7.4	12.3	12.1	10.2	10.0
	5	544.8	529.8	10.9	10.7	12.7	12.5	7.3	7.2
	6	542.7	536.4	7.5	7.4	12.2	12.0	10.1	9.9
Phase (deg.)	1	0.0	0.0	0.0	0.0	0.0	0.0	0.0	0.0
	2	-59.7	-59.8	-129.1	-129.1	-182.5	-182.5	-244.2	-244.1
	3	-120.4	-120.0	-240.1	-240.0	0.0	0.0	-119.8	-120.1
	4	-181.8	-181.7	-9.0	-8.6	-182.4	-182.5	-4.2	-4.4
	5	-240.5	-240.4	-120.0	-119.7	-0.1	0.0	-240.2	-240.5
	6	-300.0	-299.8	-248.9	-249.1	-182.5	-182.5	-124.3	-124.1

TABLE VII
COMPARISON OF RADIAL LORENZ FORCES ON STATOR COILS

Frequency (Hz)		93.34		1906.70		2000.00		2093.33	
	Slot #	FEA	PDF	FEA	PDF	FEA	PDF	FEA	PDF
Amplit-ude (N)	1	1120.4	1118.8	27.6	27.6	30.9	30.9	21.0	21.0
	2	1140.9	1139.3	23.0	23.0	29.8	29.8	26.6	26.6
	3	1121.2	1119.6	27.6	27.6	31.0	31.0	21.0	21.0
	4	1142.8	1141.2	23.0	23.0	29.9	29.9	26.6	26.6
	5	1121.1	1119.6	27.6	27.6	31.0	31.0	21.0	21.0
	6	1141.0	1139.4	23.0	23.0	29.9	29.9	26.6	26.6
Phase (deg.)	1	0.0	0.0	0.0	0.0	0.0	0.0	0.0	0.0
	2	-59.1	-59.1	214.0	214.1	169.7	169.7	99.8	99.8
	3	-120.0	-120.0	120.0	120.0	0.0	0.0	-120.0	-120.0
	4	179.4	179.4	-26.0	-26.0	169.7	169.7	-20.2	-20.2
	5	120.0	120.0	240.0	240.0	0.0	0.0	120.0	120.0
	6	60.8	60.8	94.1	94.1	169.7	169.7	-140.2	-140.2

In terms of computation efficiency, the proposed method takes a one-time overhead of 120 s to extract related PDFs and relative permeance of the motor. Then it takes 24 s to compute one operating condition of five fundamental cycles. In comparison, FEA takes 204 h for simulation and postprocessing for each operating condition.

VII. CONCLUSION AND FUTURE WORK

This article has provided a new perspective in analyzing electromagnetic forces in inverter-fed SPM motors. After demonstrating that the airgap RMF is not suitable to characterize EM forces induced by PWM current harmonics, this article has introduced an alternative method to calculate realistic EM force distributions on all actual stator components, based on the concept of PDFs. The advantages of the proposed method include the following.

1) *Clear in physical meaning:* The proposed method is based on the superposition principle of magnetic circuits. And the superposition process can be succinctly expressed in easy-to-understand matrix forms.
2) *Accurate:* For linear magnetic circuits, the proposed method is almost as accurate as the FEM in calculating EM force harmonics of all frequencies.
3) *Fast:* The proposed method utilizes the magnetostatic FEM to extract the PDFs, the rotor-PM induced flux distribution, and the relative permeance of the slotting effect for just once. All subsequent calculations are simple summations and multiplications. Therefore, the computation efficiency is several orders of magnitude faster than time-stepping FEA.

4) *Versatile:* Although this article uses a six-phase concentrated-winding SPM as an example to illustrate the principle of the method, the method can be easily extended to more complicated winding configurations, such as double-layer distributed windings, or fractional-slot windings, or other slot shapes.

Due to abovementioned advantages, the PDF-based method can be used as a powerful tool in analyzing PWM-induced vibrations of SPM motors.

In spite of aforementioned advantages, the proposed method also has several limitations.

1) The method in its current form does not account for magnetic saturations, and therefore the error on EM forces tends to increase if the studied machine is deeply saturated.
2) The method in its current form requires the rotor to be approximately nonsalient, and therefore limiting its usage to SPM motors.

In the future, more studies will be done to address the limitations of the proposed method.

REFERENCES

[1] S. M. Raziee, O. Misir, and B. Ponick, "Multiple multiphase combined star–polygon winding analysis," *IEEE Trans. Ind. Electron.*, vol. 66, no. 10, pp. 7468–7479, Oct. 2019.

[2] A. S. Abdel-Khalik, S. Ahmed, and A. M. Massoud, "A nine-phase six-terminal concentrated single-layer winding layout for high-power medium-voltage induction machines," *IEEE Trans. Ind. Electron.*, vol. 64, no. 3, pp. 1796–1806, Mar. 2017.

[3] F. Scuiller, J. Charpentier, and E. Semail, "Multi-star multi-phase winding for a high power naval propulsion machine with low ripple torques and high fault tolerant ability," in *Proc. IEEE Veh. Power Propulsion Conf.*, 2010, pp. 1–5.

[4] Bojoi R *et al.*, "Multiphase electrical machines and drives in the transportation electrification," in *Proc. IEEE 1st Int. Forum Res. Technol. Soc. Ind. Leveraging Better Tomorrow* Turin, Italy, 2015, pp. 205–212.

[5] W. C. Lo, C. C. Chan, Z. Q. Zhu, Lie Xu, D. Howe, and K. T. Chau, "Acoustic noise radiated by PWM-controllel induction machine drives," *IEEE Trans. Ind. Electron.*, vol. 47, no. 4, pp. 880–889, Aug. 2000.

[6] X. Han, D. Jiang, T. Zou, R. Qu, and K. Yang, "Two-Segment three-phase PMSM drive with carrier phase-shift PWM for torque ripple and vibration reduction," *IEEE Trans. Power Electron.*, vol. 34, no. 1, pp. 588–599, Jan. 2019.

[7] Y. Huang, Y. Xu, Y. Li, G. Yang, and J. Zou, "PWM frequency voltage noise cancelation in three-phase VSI using the novel SVPWM Strategy," *IEEE Trans. Power Electron.*, vol. 33, no. 10, pp. 8596–8606, Oct. 2018.

[8] N. Kurihara, J. Bayless, H. Sugimoto, and A. Chiba, "Noise reduction of switched reluctance motor with high number of poles by novel simplified current waveform at low speed and low torque region," *IEEE Trans. Ind. Appl.*, vol. 52, no. 4, pp. 3013–3021, Jul./Aug. 2016.

[9] J. Le Besnerais, V. Lanfranchi, M. Hecquet, and P. Brochet, "Characterization and reduction of audible magnetic noise due to PWM supply in induction machines," *IEEE Trans. Ind. Electron.*, vol. 57, no. 4, pp. 1288–1295, Apr. 2010.

[10] J. Besnerais, V. Lanfranchi, M. Hecquet, and P. Brochet, "Characterization and reduction of audible magnetic noise due to PWM supply in induction machines," *IEEE Trans. Ind. Electron.*, vol. 57, no. 4, pp. 1288–1295, Apr. 2010.

[11] W. Deng and S. Zuo, "Axial force and vibroacoustic analysis of external-rotor axial-flux motors," *IEEE Trans. Ind. Electron.*, vol. 65, no. 3, pp. 2018–2030, Mar. 2018.

[12] H. C. Dirani, A. Merkhouf, A. Giroux, B. Kedjar, and K. Al-Haddad, "Impact of real air-gap nonuniformity on the electromagnetic forces of a large hydro-generator," *IEEE Trans. Ind. Electron.*, vol. 65, no. 11, pp. 8464–8475, Nov. 2018.

[13] D. Zarko, D. Ban, and T. A. Lipo, "Analytical calculation of magnetic field distribution in the slotted air gap of a surface permanent-magnet motor using complex relative air-gap permeance," *IEEE Trans. Mag.*, vol. 42, no. 7, pp. 1828–1837, Jul. 2006.

[14] L. J. Wu, Z. Q. Zhu, D. Staton, M. Popescu, and D. Hawkins, "An improved subdomain model for predicting magnetic field of surface-mounted permanent magnet machines accounting for tooth-tips," *IEEE Trans. Mag.*, vol. 47, no. 6, pp. 1693–1704, Jun. 2011.

[15] H. Yang and Y. Chen, "Influence of radial force harmonics with low mode number on electromagnetic vibration of PMSM," *IEEE Trans. Energy Convers.*, vol. 29, no. 1, pp. 38–45, Mar. 2014.

[16] Z. Q. Zhu, Z. P. Xia, L. J. Wu, and G. W. Jewell, "Analytical modeling and finite-element computation of radial vibration force in fractional-slot permanent-magnet brushless machines," *IEEE Trans. Ind. Appl.*, vol. 46, no. 5, pp. 1908–1918, Sep./Oct. 2010.

[17] L. Hu, K. Yang, C. Suo, Y. Ding, and W. Yu, "Analysis of radial electromagnetic force in permanent magnet machine with manufacturing tolerance," in *Proc. 21st Int. Conf. Elect. Mach. Syst.*, Jeju, South Korea, 2018, pp. 256–260.

[18] F. Magnussen and H. Lendenmann, "Parasitic effects in PM machines with concentrated windings," *IEEE Trans. Ind. Appl.*, vol. 43, no. 5, pp. 1223–1232, Sep./Oct. 2007.

Yajun Lv was born in Baoji, China, in 1994. He received the B.S. degree in electrical engineering from Xi'an Jiaotong University, Xi'an, China, in 2016, and the M.S. degree in electrical engineering in 2018 from the Naval University of Engineering, Wuhan, China, where he is currently working toward the Ph.D. degree with the National Key Laboratory of Science and Technology on Vessel Integrated Power System.

His current research interests include vibration analysis of permanent-magnet synchronous machines.

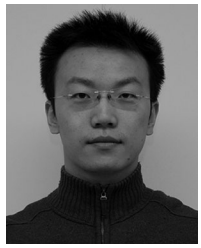

Siwei Cheng (Member, IEEE) was born in Wuhan, China, in 1985. He received the B.S. degree in electrical engineering from Tsinghua University, Beijing, China, in 2007, and the M.S. and Ph.D. degrees in electrical engineering from the Georgia Institute of Technology, Atlanta, GA, USA, in 2009 and 2012, respectively.

From 2012 to 2013, he was with the Hybrid/Electric Vehicle Team, Ford Motor Company, Dearborn, MI, USA, as a Motor Control Engineer. Since 2014, he has been with the Naval University of Engineering, Wuhan, China, where he is currently an Associate Professor of electrical engineering. His research interests include the design, control, and condition monitoring of electric machines and computational intelligence and signal processing techniques applied to energy system and electric propulsion system.

Zhongkun Ji was born in Beijing, China, in 1995. He received the B.S. degree in electrical engineering in 2017 from the Naval University of Engineering, Wuhan, China, where he is currently working toward the Ph.D. degree with the National Key Laboratory of Science and Technology on Vessel Integrated Power System.

His current research interests include control of permanent-magnet synchronous machines.

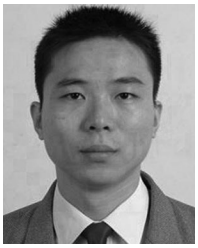

Dong Wang (Member, IEEE) was born in Wuhan, China, in 1978. He received the B.Eng. and Ph.D. degrees in electrical engineering from the Naval University of Engineering, Wuhan, China, in 2000 and 2007, respectively.

He is currently a Professor and a Supervisor for doctoral candidates with the Naval University of Engineering. His research interests include electric propulsion and integrated power generation systems.

Junquan Chen (Member, IEEE) received the B.Eng. and Ph.D. degrees in electrical engineering from the Naval University of Engineering, Wuhan, China, in 2006 and 2013, respectively.

He is currently an Associate Professor with the Naval University of Engineering. His research interests include modeling and measurement of magnetic materials, design, and multiphysics analysis of electrical machines.